Article



Calcium-induced environmental adaptability of the blood protein vitronectin

Ye Tian, ¹ Kyungsoo Shin, ¹ Alexander E. Aleshin, ¹ Wonpil Im, ² and Francesca M. Marassi^{1,*}
¹Sanford Burnham Prebys Medical Discovery Institute, La Jolla, California and ²Departments of Biological Sciences, Chemistry, and Bioengineering, Lehigh University, Bethlehem, Pennsylvania

ABSTRACT The adaptability of proteins to their work environments is fundamental for cellular life. Here, we describe how the hemopexin-like domain of the multifunctional blood glycoprotein vitronectin binds Ca²⁺ to adapt to excursions of temperature and shear stress. Using X-ray crystallography, molecular dynamics simulations, NMR, and differential scanning fluorimetry, we describe how Ca²⁺ and its flexible hydration shell enable the protein to perform conformational changes that relay beyond the calcium-binding site and alter the number of polar contacts to enhance conformational stability. By means of mutagenesis, we identify key residues that cooperate with Ca²⁺ to promote protein stability, and we show that calcium association confers protection against shear stress, a property that is advantageous for proteins that circulate in the vasculature, like vitronectin.

SIGNIFICANCE Vitronectin (Vn) plays important roles in cell adhesion and migration, bone remodeling, and immunity. It circulates in blood but is also found in the extracellular matrix and accumulates with the plaques associated with agerelated macular degeneration, Alzheimer's disease, atherosclerosis, and other disorders of aging. Here, we show that calcium helps Vn adapt its conformation to diverse environmental conditions, such as temperature and shear flow. The results shed light on the way in which Vn adapts to its surroundings. This structural knowledge is important for the development of diagnostic, preventive, or therapeutic approaches.

INTRODUCTION

Proteins in the vasculature are particularly adept at functioning in a diverse range of chemical and physical conditions. Vitronectin (Vn), for example, circulates in blood at a concentration of 0.2–0.5 mg/mL as a major plasma protein (1-3) and as a component of high-density lipoprotein (4,5)but also associates with the extracellular matrix through its collagen-binding and heparin-binding domains (6). Vn interacts with multiple ligands to regulate diverse physiological processes: it employs its Arg-Gly-Asp sequence to bind integrin receptors and promote cell adhesion, spreading, and migration (7); it regulates hemostasis through the interactions of its somatomedin B domain with type 1 plasminogen activator inhibitor (8); it controls complement-mediated pore formation and cell lysis through the interactions of its C-terminal domain with the C5b-C9 components of the membrane attack complex (9); and it is recruited by many pathogens to acquire protection from

Submitted March 19, 2022, and accepted for publication August 29, 2022.

*Correspondence: fmarassi@sbp.edu

Editor: Wendy Shaw.

https://doi.org/10.1016/j.bpj.2022.08.044

© 2022 Biophysical Society.

complement-mediated lysis (10). While Vn is synthesized primarily in the liver, it is also expressed in retina (11–13), brain (14), and vascular smooth muscle cells (15). Moreover, Vn expression is upregulated in a number of diseases, including atherosclerosis (16), Alzheimer's disease (17–19) and age-related macular degeneration (19,20). In these settings, Vn is often associated with calcified protein-lipid deposits that accumulate with disease progression (21), but its specific role in calcified deposit formation is not well understood.

Previously, we determined the three-dimensional structure of the hemopexin-like (HX) domain of Vn (22) and showed that it acquires substantial thermodynamic stability upon binding either soluble ionic calcium ($\mathrm{Ca^{2+}}$) or mineralized hydroxyapatite [$\mathrm{Ca_{10}}(\mathrm{PO_4})_6(\mathrm{OH})_2$]—the major inorganic component of pathological calcified protein-lipid deposits (23). Here we describe the structural mechanism for this calcium-dependent effect and show that it also confers Vn-HX with mechanical stability against shear stress, such as that encountered in the vasculature. Calcium association with key Vn residues stabilizes protein states with subtly different conformations and levels of hydration. These



results are important for understanding the roles of Vn in health and disease and also illustrate a fundamental mechanism of environmental adaptation.

MATERIALS AND METHODS

Protein preparation

The HX domain sequence encompasses Vn residues 154-285, 324-354, and 435-474 and includes the four repeat sequences that make up four blades of the Vn-HX β-propeller. Two flexible or disordered segments (residues 286-323 and 355-434) were deleted, and two mutations (C180S, C215S) were introduced, to facilitate protein refolding and crystallization. In addition to wild-type, we examined three mutant sequences: mD (D162N, D207N, D255N, and D347N), mD13 (D162N and D255N), and mD24 (D207N and D347N). Wild-type and mutant Vn-HX were prepared from E. coli as described (22), with minor modifications. Briefly, the insoluble protein fraction was isolated from the cell lysate in guanidine-containing buffer (20 mM Tris-HCl [pH 8], 6 M guanidine, 10 mM DTT), and the protein was refolded at 4°C, by dropwise dilution from an initial concentration of 2-3 mg/mL in guanidine, to a final concentration of 0.1 mg/mL in folding buffer (20 mM Tris-HCl [pH 8], 500 mM ArgCl, 300 mM CaCl₂, 5 mM β-mercaptoethanol, 1 mM hydroxyethyldisulfide). After 72 h of gentle stirring followed by dialysis against final buffer (20 mM MES buffer [pH 6.5], 300 mM NaCl), the protein solution was concentrated with a 10 kDa cutoff Vivaspin 20 device (GE Healthcare, Chicago, IL, USA), then purified by size-exclusion chromatography (Superdex 200 10/300 GL, GE Healthcare). The yield of purified folded protein is in the range of 10 mg per liter of cell culture for wild-type, mD13, and mD24 proteins and 1 mg per liter of culture for the mD mutant. Proteins produced in E. coli lack the sugars that normally decorate human Vn at residues N169 and N242.

Crystallization, X-ray data acquisition, and structure determination

A solution of Vn-HX (6 mg/mL) was dialyzed overnight into buffer A (20 mM MES [pH 6.5], 100 mM NaCl, and 1 mM CaCl₂) and then cleared by centrifugation. The final protein concentration was 4 mg/mL. Crystals were obtained by mixing 0.2–0.3 μ L Vn-HX (4 mg/mL in buffer A) with $0.15 \mu L$ of precipitant solution (20 mM MES [pH 6.5], 90 mM imidazole, 30 mM NaNO₃, 30 mM Na₂HPO₄, 30 mM (NH₄)₂SO₄, 11.25% (v/v) 2-methyl-2,4-pentanediol, 11.25% (w/v) PEG-1000, 11.25% (w/v) PEG-3350, and 3% (w/v) d-(+)-trehalose), and then equilibrating in a sitting drop plate with 50 μ L of precipitant solution at room temperature. Crystals appeared within a week and grew for an additional 2-3 weeks. To analyze metal ion binding, the crystals were soaked overnight with 1, 100, or 200 mM CaCl₂ or 50 mM KCl in Na⁺-free soaking solution (20 mM Bis-Tris methane-Cl [pH 6.5], 70 mM NH₄NO₃, 11.25% (v/v) 2-methyl-2,4-pentanediol, 11.25% (w/v) PEG-1000, 11.25% (w/v) PEG-3350, and 3% (w/v) d-(+)-trehalose). Soaking with KCl solution destroyed the crystals. The CaCl2-soaked crystals were flash frozen in liquid nitrogen and shipped to the Stanford Synchrotron Radiation Lightsource for data collection.

X-ray diffraction data were collected at the Stanford Synchrotron Radiation Lightsource beamline BL12-2 at a wavelength of 0.97946 Å and a temperature of 100 K. The data were processed using the CCP4 suite (24). The structure from a crystal treated with 1 mM CaCl₂ (Vn-Ca₁) was solved first by molecular replacement of the previously published (22) Na⁺-bound structure (Vn-Na₁; PDB: 6O5E; 100% identity) and then was used to solve other structures. The structures were manually corrected in Coot (25) and refined by Refmac5 (26). Comparison of the structures soaked with various CaCl₂ concentrations did not reveal significant differences in binding of metal ions. Molprobity (27) and the PDB validation

server were used for structure validation throughout refinement. All structures had Ramachandran statistics with more than 95% of residues in favored positions and less then 1% outliers. The data collection and refinement statistics are presented in Table S1. The structure coordinates were deposited in the PDB with accession codes PDB: 7TXR (Vn-Ca₁), 7RJ9 (Vn-Ca₂), and 7U68 (Vn-Na₂).

NMR spectroscopy

The NMR samples were prepared as described (22). NMR experiments were performed at 30°C on a Bruker Avance 600 MHz spectrometer equipped with a $^{1}\text{H}/^{13}\text{C}/^{15}\text{N}$ triple-resonance cryoprobe. The NMR data were processed and analyzed using TopSpin (Bruker, Billerica, MA, USA). Assignments of the ^{1}HN and ^{15}N chemical shifts were transferred from the previously assigned data for HX with Na⁺ or Ca²⁺ (22) (BMRB: 50241 and 50261).

Differential scanning fluorimetry (DSF) experiments

Protein-melting experiments were performed in a 96-well plate format, using a LightCycler 480 instrument (Roche, Basel, Switzerland), with a linear temperature gradient of 0.03°C/s from 20°C to 95°C as described previously (22).

Shear stress experiments

Methods were adapted from published protocols (28,29). Protein solutions were prepared in a 150 μL volume, with 12 μM Vn-HX, 20 mM MES (pH 6.5), 30 mM NaCl, and an additional 8 mM NaCl or 8 mM CaCl $_2$. Shear force was applied using a 27G needle with an internal diameter of 0.21 mm and a length of 12.7 mm, fitted to a 1 mL syringe. For each 1 s syringe stroke, the protein solution was drawn and extruded through the needle to produce $\sim\!\!750$ dynes/cm 2 per stroke. After 30 repetitive syringe strokes, insoluble protein aggregates were removed by centrifugation (17,000 \times g, 5 min), and the remaining soluble protein concentration was estimated by measuring UV absorbance (280 nm).

Molecular dynamics (MD) simulations

All-atom MD simulations were performed as described (30), using the CHARMM36 force fields (31) with the TIP3P water model (32). The temperature was set to 303.15 or 333.15 K for simulations at 30°C or 60°C, respectively, and the pressure was maintained at 1 bar. All systems for MD (Table S3) were identical to the experimental protein sequences to enable cross-comparisons. The systems were prepared and equilibrated using CHARMM-GUI Solution Builder (33). The initial structural models were generated from the crystal structure of Vn-Na₁ (PDB: 605E, molecule A). All ligands and water molecules were removed, and residues with missing electron density were modeled using GalaxyFill (34). For the Ca²⁺-bound simulations, Na⁺ ions were replaced with Ca²⁺, and the models were solvated in a cubic water box and then equilibrated with the CHARMM-GUI standard protocol for 125 ps before the production runs.

MD production simulations were conducted with OpenMM (35) for 1 μ s, and the last 500 ns of trajectories were used for analysis. Five 1 μ s MD simulations were performed for each of four wild-type Vn-HX systems bound to Na⁺ or Ca²⁺ (Vn-Na and Vn-Ca), at 30°C or 60°C, and for each of three mutant systems bound to Ca²⁺ (mD-Ca, mD13-Ca, and mD24-Ca), at 30°C, for a total of 35 independent simulations (Table S3). Four additional 3.2 μ s simulations were performed at 30°C for each of four wild-type Vn-HX systems with different Na⁺ and Ca²⁺ ion combinations at the m1 and m2 metal ion binding sites.

For each simulation, trajectories were generated every 1 ns, and trajectories from all simulations were combined for analysis in each system. Statistical analyses were performed with home-made Python scripts in MDAnalysis and JupyterNotebook.

RESULTS AND DISCUSSION

Structure of calcium-bound Vn-HX domain

To resolve the calcium binding site of the HX domain, we determined two structures, each from a crystal treated with 1 mM CaCl₂ (Vn-Ca₁) or 100 mM CaCl₂ (Vn-Ca₂). The structures refined to a resolution of 2.0 and 1.7 Å, respectively (Table S1). They have the same crystallographic space group as the previously determined (22) sodium-bound structure (Vn-Na₁), but Vn-Ca₂ has different unit cell parameters and different crystal packing. Soaking the Vn-Ca₂ crystal with EDTA yielded a second sodium-bound and calcium-free structure (Vn-Na₂), with the same space group and unit cell parameters as Vn-Ca₂ and a resolution of 2.0 Å. In all structures, the crystallographic asymmetric unit contains two copies of the protein molecule. The Vn-Ca₂ and Vn-Na₂ structures are representative of the differences between Ca²⁺- and Na⁺-bound states (Fig. 1).

Vn-HX maintains its canonical four-bladed β/α propeller with either Ca²⁺ or Na⁺. Each of the four HX repeats corresponds to one propeller blade (β 1- β 2- β 3- α), and the propeller is circularized by a C156-C472 disulfide bond that connects the termini (Fig. 1 *A* and *B*). The propeller top—defined here as the N-terminal end of the β 1 strands—forms a smooth surface, while loops of variable lengths protrude from the bottom, including two flexible regions spanning residues 283–324 and 354–435, which were deleted to facilitate refolding and crystallization (22). The propeller bottom has overall higher B factors and some missing electron density for the more flexible regions (Table S2).

The four $\beta 1$ strands form a channel (Figs. 1 *C–F* and S1) that occludes a NaCl molecule, with Na⁺ and Cl⁻ coordinated by the backbone carbonyl oxygens (Na⁺; metal binding site m2) and amide hydrogens (Cl⁻) of β1 residues F164, A209, A257, and A349. The m2 site is occupied by Na⁺ in all structures, even after soaking the crystals with 100-200 mM CaCl₂ in sodium-free buffer. The D162, D207, D255, and D347 (rim-Asp) side chains extend from the top rim of the channel to form an electronegative pole (22,23), and their backbone carbonyl oxygens coordinate Ca²⁺ or Na⁺ (metal binding site m1). In the calcium-bound states, the Ca²⁺ coordination sphere is completed by three (Vn-Ca₂) to four (Vn-Ca₁) water molecules (Figs. 1 C and E and S1 A-D). Several of these waters are within 3.2 Å of the rim-Asp carboxyl oxygens and establish a watermediated H-bond network involving the rim-Asp side chains, water, and Ca²⁺. In the sodium-bound states (Figs. 1 D and F and S1 E-H) by contrast, Na⁺ is either not hydrated (Vn-Na₂) or bound to a single water molecule (Vn-Na₁). Calcium ion ligation at m1 is supported by several observations: agreement of the coordination stereochemistry with known parameters specific for Ca²⁺ (36,37), marked increase in electron density relative to Na⁺, and temperature B factors consistent with those of the protein and water donor atoms (Table S2). In proteins, Ca²⁺ is generally coordinated by seven oxygen atoms (typically neutral, carboxylate, or water oxygen) in a conformation best represented by a pentagonal bipyramid (37), and this is what's observed for the Vn-HX domain (Fig. S1). As predicted by NMR (23), the Ca²⁺ ion is not deeply buried within the channel and locates 0.4–0.8 Å further away from Cl⁻ and the m1 Na⁺ ions (Figs. 1 *C–F* and S1).

The Ca²⁺ and Na⁺ structures differ at the propeller top, where the Q345 and D255 side chains form a salt bridge in the presence of Ca²⁺ but splay apart with Na⁺ (Fig. 1 A). This is accompanied by a backbone rearrangement in the HX4 blade and is consistent with the calcium-induced perturbations that we observed in the NMR signals of D255 and Q345 (23). The structures also differ at the bottom of the propeller, where m2-occluded Na+ is stabilized either by the D166 carboxylate side chain or a sulfate anion (Figs. 1 C and E and S1). In the sulfate-free molecule of Vn-Ca₂ (Fig. 1 C), the D166 side chain reaches deep inside the channel, establishing ~ 0.5 Å closer contacts between its carboxylate anion and m2 Na⁺, resulting in a D166-capped conformation of the channel. In sulfate-bound Vn-Ca₂ (Figs. 1 E and S1 D), the sulfate anion arranges to form close contact with Na⁺ as well as favorable polar contacts with the backbone amide hydrogens of D166, T211, A259, and A351. This releases the K168 side chain from the channel opening, making the channel bottom more accessible to solvent. In Vn-Ca₁, by contrast (Fig. S1 B), the sulfate anion adopts a different arrangement in the protein channel (also observed in Vn-Na₁ and Vn-Na₂) such that polar contacts to the protein backbone are replaced by contacts to the K168 side chain, which reaches into the channel. Taken together, the structures illustrate the conformational plasticity of Vn-HX and its response to Ca^{2+} .

Effect of calcium on the Vn-HX channel

Previously, we showed that Ca^{2+} binds Vn-HX with a dissociation constant in the range of 27 μ M (23). Since this value is approximately ten times higher than the blood concentration of Vn (2.5–5 μ M) (1–3) and thirty times lower than the total blood concentration of Ca^{2+} (1.3–1.5 mM) (37), we concluded that Vn is calcium bound in vivo. Using NMR, we showed that Ca^{2+} enhances the conformational exchange dynamics of Vn on the millisecond timescale, and by monitoring protein unfolding with DSF and an environment-sensitive fluorescent dye, we showed that Ca^{2+} markedly increases the unfolding transition temperature of Vn and thus protects the structure from thermal denaturation.

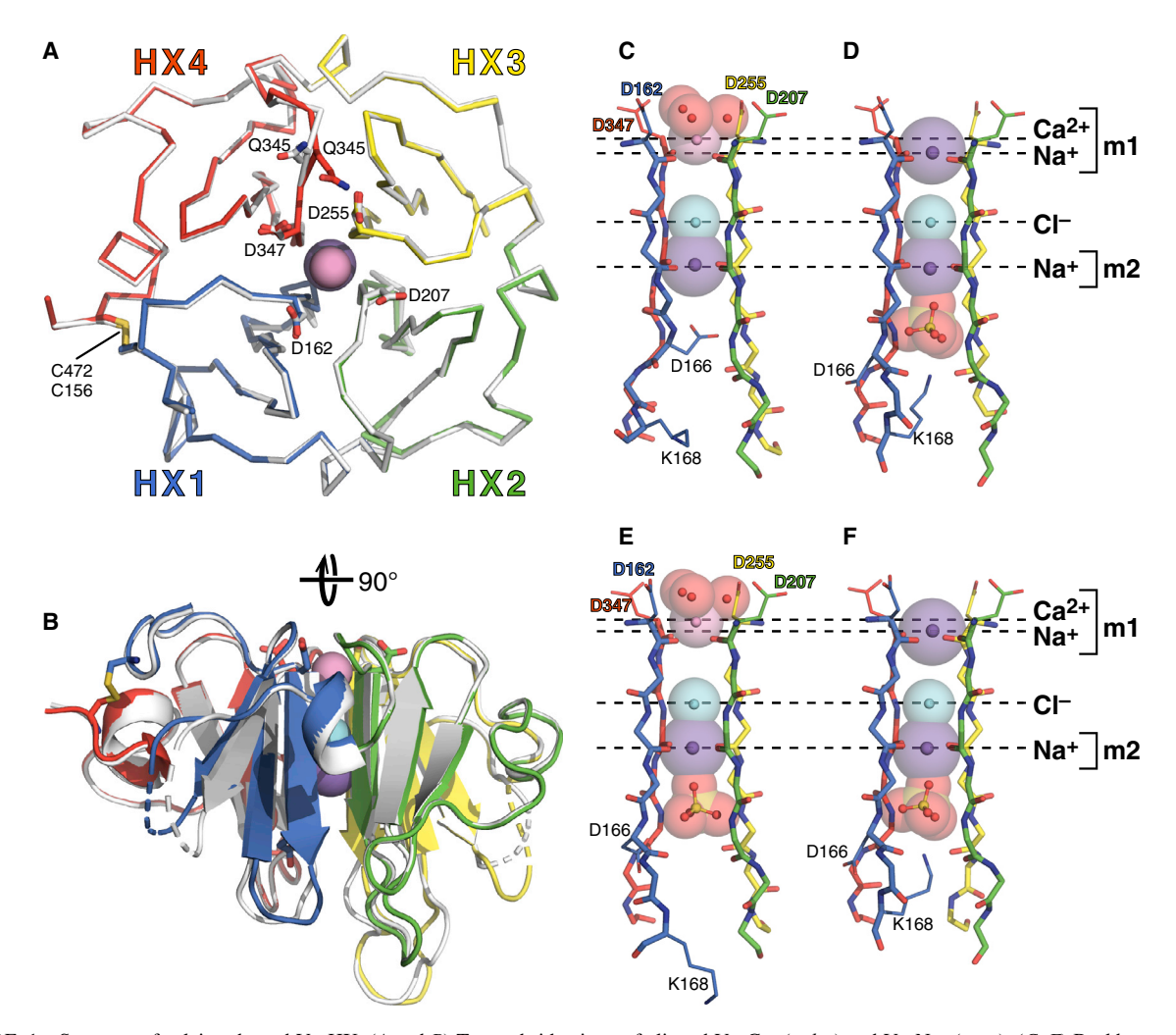


FIGURE 1 Structure of calcium-bound Vn-HX. (A and B) Top and side views of aligned Vn-Ca₂ (c (c olor) and Vn-Na₂ (g (r ay). (C-F) Backbone representations of the channel structures of Vn-Ca₂ (C and E) and Vn-Na₂ (D and F). Molecules A (C and D) and B (E and F) of the asymmetric unit are shown for each structure. Dashed horizontal lines mark the positions of Ca²⁺, Na⁺, and Cl⁻. Colors denote structural repeats HX1 (blue), HX2 (green), HX3 (yellow), and HX4 (red). Spheres denote Na⁺ (red), Cl⁻ (req), Cl⁻ (req), O (red), or S (rellow). Broken loops denote gaps in the protein chain due to missing electron density. Sticks denote key side chains, disulfide-linked Cys, and the backbone of the central channel. To see this figure in color, go online.

These effects are specific for Ca^{2+} and not observed for other metal ions $(Na^+, K^+, Zn^{2+}, Mg^{2+}, and Ni^{2+})$.

To understand the molecular basis for these calcium-specific effects, we performed unrestrained all-atom MD simulations of Vn-HX with Ca²⁺ (Vn-Ca) or Na⁺ (Vn-Na), at 30°C or 60°C (Table S3). These temperatures were selected to match the experimental temperature of our NMR studies (30°C) and as the point where Na⁺-bound Vn-HX is 50% unfolded while Ca2+-bound Vn-HX is still fully folded (60°C). The starting structure of Vn-Ca was generated by modeling short regions of missing electron density in the Vn-Na₁ crystal structure (PDB: 6O5E, molecule A) and explicitly replacing Na⁺ with Ca²⁺ in the m1 site while keeping Na⁺ at m2. A 3.2 µs MD simulation shows that Ca²⁺ remains bound to the protein over this time course, with little fluctuation in its starting position at an average distance of 5.4 Å from the channel-occluded Cl⁻ anion (Fig. S2 A). By contrast, an alternative model where Na⁺

was replaced with Ca^{2+} at the m2 site results in unstable association of either Ca^{2+} or Na^+ with the m1 site (Fig. S2 *B*). These results are in agreement with the previous NMR data (23) and the new crystal structures, which all identify m1 as the Ca^{2+} -binding site.

Five independent 1 μ s MD simulations of Vn-Ca or Vn-Na result in average conformations and positions of the channel ions that mirror the experimental structures (Fig. 2 A–C). Ca²⁺ binds higher in the channel (\sim 5.4 Å from Cl $^-$) than Na $^+$ (4.9 Å from Cl $^-$) and exhibits a narrower range of positional fluctuation at both temperatures. Ca²⁺ is also more solvent exposed and coordinates an average of four (30°C) or three (60°C) water molecules (Figs. 2 D–F and S3 A), compared with 1.5 water molecules associated with Na $^+$ at either temperature.

At 30°C, the D166 side chain exhibits predominantly two conformations in either Vn-Ca or Vn-Na: a closed conformation (Fig. 2 *D*), with the D166 carboxylate group capping

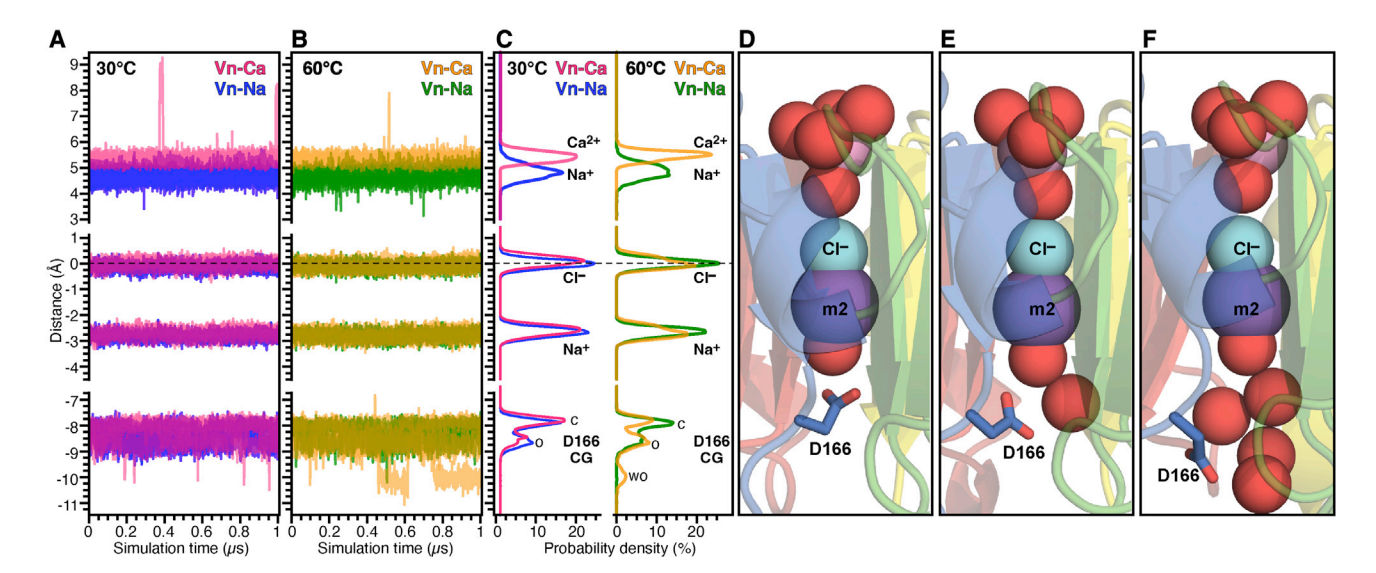


FIGURE 2 MD simulations of atomic positions within the Vn-HX channel. Distances of Na⁺, Ca²⁺, and the D166 CG atom are relative to the average position of Cl⁻ in the channel. (A and B) Time series of atomic positions for five independent 1 µs MD simulations. (C) Average probability distributions of the atomic distances extracted from the time-dependent data. Each distribution is the average over the last 500 ns of five independent 1 μ s simulations. Colors denote MD data for Vn-Ca at 30°C (pink) or 60°C (yellow) and Vn-Na at 30°C (indigo) or 60°C (green). D166 closed (c), open (o), and wide open (wo) conformations are marked. (D-F) MD simulation snapshots of Vn-Ca at 30°C, showing closed (D), open (E), and wide-open (F) conformations of D166. Structural model color scheme as in Fig. 1. To see this figure in color, go online.

the channel bottom as in the sulfate-free crystal structures, and an open conformation (Fig. 2 E), with the channel more accessible to solvent. Increasing the temperature to 60°C equalizes the closed and open populations of D166 in Vn-Ca and populates a third, wide-open conformation (Fig. 2 F) where D166 points away from the channel. The conformational profile of Vn-Na, by contrast, is not appreciably affected by temperature.

Calcium modulates the conformational adaptation to temperature of Vn-HX

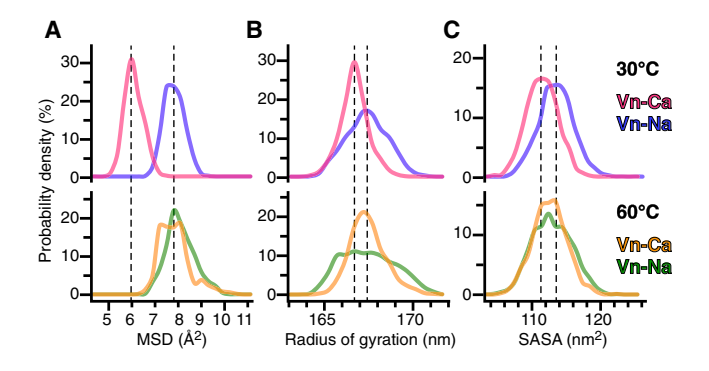
The mean-square displacement (MSD) of atomic coordinates from the starting model reflects protein flexibility, while the radius of gyration and solvent accessible surface area provide estimates of protein compactness, all properties that are associated with protein adaptation to temperature (38,39). The average MSD values from the four sets of MD simulations, with Ca²⁺ or Na⁺, demonstrate a distinct effect of Ca²⁺: while Vn-Na has equivalent MSDs at 30°C and 60°C, the MSD of Vn-Ca is distinctly lower at 30°C but shifts within the range of Vn-Na at 60°C (Figs. 3 A and S3 B).

Temperature also has a marked effect on the compactness of Vn-Ca but no appreciable effect on Vn-Na (Figs. 3 B and C and S3 C and D): at 30°C, Ca^{2+} reduces both the radius of gyration and solvent accessible surface area, while both parameters return to the levels of Vn-Na at 60°C and are visibly sharper for Vn-Ca at both temperatures. The calcium-dependent temperature profile is also mirrored by the average number of water molecules found within 4 Å of the m1 metal ion: while temperature has a large effect on the water coordination of Ca²⁺ at m1, little difference is observed for Na⁺ (Fig. S3 A). Overall, the data indicate that Ca²⁺ enhances the protein's adaptability to temperature, rendering it able to alter its flexibility compactness and hydration with temperature alteration.

The Ca²⁺-dependent temperature adaptability property is further reflected in the conformational response of Vn-HX to temperature. At 30°C, Ca²⁺ favors cross-sectional HX1-HX3 interatomic distances (Fig. 3 D and E) that are \sim 1 Å greater than Vn-Na at the channel top and smaller at the bottom. At the top of the channel, Ca²⁺ also broadens the interatomic distance distribution profile, indicating that it increases the range of conformations that the channel can sample on the μ s timescale of the simulation. At 60°C, the effect of Ca²⁺ is reversed, favoring cross-sectional distances that are smaller at the channel top and greater at the bottom, and while the HX2-HX4 distances are much less susceptible to Ca²⁺, they too change slightly in the same temperature-dependent directions. By contrast, temperature has little effect on the conformation of Vn-Na, where the channel size does not vary between 30°C and 60°C.

Correlation between polar contacts and thermal stability

To further examine protein conformation, we calculated the number of polar contacts-including H-bonds and salt bridges-mediated by no more than one water molecule (Table S4). At 30°C, Ca²⁺ increases the average total



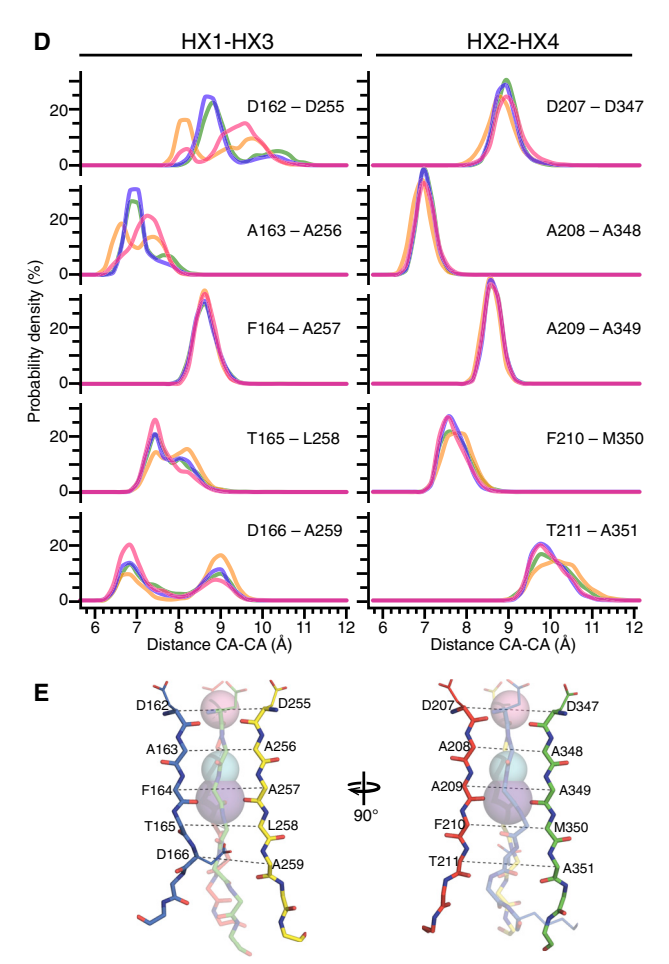


FIGURE 3 MD simulations of protein flexibility, compactness, and HX channel conformation. (A–D) Probability distributions of MSD (A), radius of gyration (B), solvent accessible surface area (C), and cross-channel CA atom distances (D). Each distribution reflects the average over the last 500 ns of five independent 1 µs MD simulations. MD data color scheme as in Fig. 2. (E) Orthogonal views of the channel backbone in the structure of Vn-Ca₂ (molecule A of the asymmetric unit). Colors are as in Fig. 1. Dashed lines connect cross-channel HX1-HX3 and HX2-HX4 CA atoms. Structural model color scheme as in Fig. 1. To see this figure in color, go

number of polar contacts by ~ 3 compared with Na⁺ (Table S4; Fig. 4 A), affecting predominantly residues in the channel-juxtaposed HX1 and HX3 blades (Fig. S4). For example, examination of the MD structural models reveals that Ca²⁺ promotes the formation of contacts (D162-R176, D184-R189, D248-R324) situated longitudinally from propeller top to bottom in blades HX1 and HX3 (Fig. 4 B and C). At 30°C, Ca^{2+} also favors the formation of polar contacts between the D166 carboxylate and the backbone atoms of its surrounding residues (T211, A259, A351) the bottom of the channel (Fig. 4 B), and this has the effect of populating the closed conformation of D166 described above (Fig. 2). Increasing the temperature to 60°C reduces the overall number of polar contacts for both Vn-Ca and Vn-Na, but here too, Vn-Ca has ~ 0.3 more contacts than Vn-Na.

Finally, Ca²⁺ association induces the formation of a water-bridged network involving the rim-Asp carboxylates and the Ca²⁺ cation, in agreement with the crystal structures. In line with this observation, the distribution of water residence times within the 5 Å periphery of the m1 metal ion is shifted toward longer times in the presence of Ca²⁺ compared with Na⁺ (Fig. 4 D). At 30°C with Na⁺, 99% of water molecules reside within 5 Å of m1 for <1.5 ns, and none reside longer than 2.5 ns. With Ca^{2+} , however, $\sim 10\%$ of water molecules remain in the 5 Å periphery of m1 longer than 2.5 ns, and \sim 5% have residence times as long as 10 ns. At 60°C, the effect of Ca²⁺ on water residence time is attenuated but still evident (\sim 9% residence for >2.5 ns, 4% as long as 10 ns). The data indicate that the water network associated with Ca²⁺ exchanges less rapidly with bulk solvent on the μ s timescale of MD simulations.

The enrichment of polar interactions is a key source of folding stability and lower heat capacity of unfolding in thermophilic proteins (40-42). In the case of Vn-HX, the MD simulations indicate that Ca²⁺ increases the average number of direct and water-mediated polar contacts relative to Na⁺. To estimate the difference in unfolding free energy (ΔG) between the Ca²⁺- and Na⁺-bound states of the protein, we used the generic stability curve equation (Eq. 1) developed by Rees and Robertson (42):

$$\Delta G(T) = [2.9N + 0.058N(T_m - 333)][(T_m - T) / T_m]$$

$$-0.058N\{T_m - T[1 - ln(T/T_m)]\} kJ/mol,$$
 (1)

where T is the ambient temperature, $\Delta G(T)$ is the free energy of unfolding, N is the number of protein residues (N = 204 for Vn-HX), and T_m is the temperature of unfolding. Based on the experimental values of T_m that we measured with DSF for Vn-HX with Ca²⁺ or Na⁺ (Table S5), the estimates of $\Delta G(T)$ indicate that 2 mM Ca^{2+} confers extra stability against unfolding of ~ 2.7 kcal/mol at 30°C and ~3.0 kcal/mol at 60°C, relative to Na⁺ (Fig. 4 A; Table S5). These estimates are within the range determined for thermophilic proteins that acquire thermal stability by increasing their polar contacts (42).

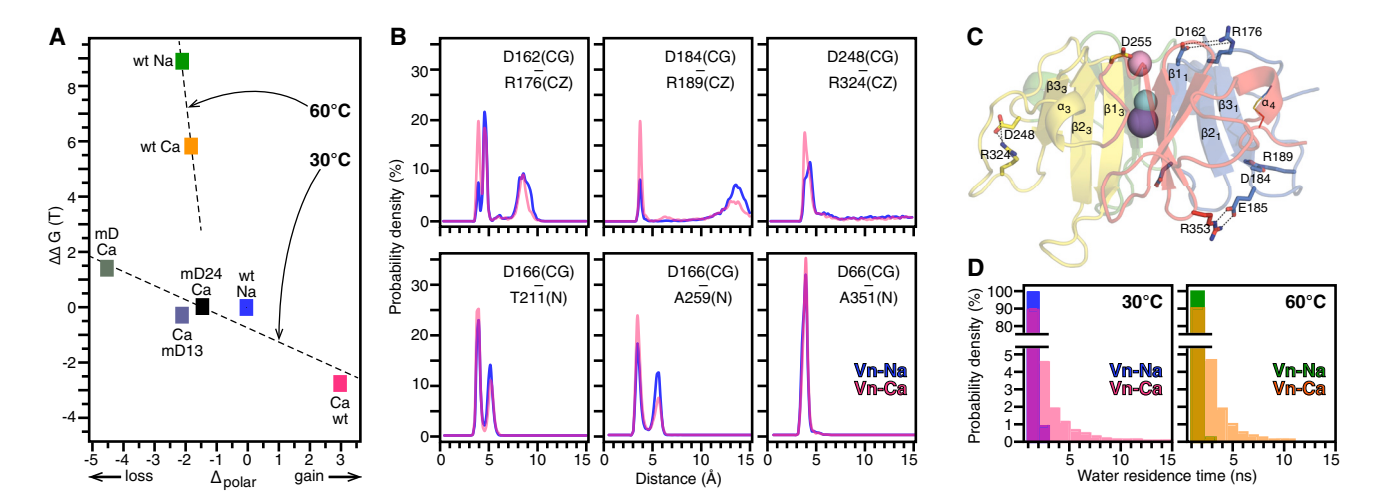


FIGURE 4 Effect of Ca^{2+} on the number of polar contacts from MD simulations. (A) The change in number of polar contacts (Δ_{polar}) estimated from MD simulations, tracks with values of $\Delta\Delta G$ estimated from the experimental values of T_m (Tables S4 and S5) with Eq. 1. Values for calcium-bound protein reflect DSF measurements with 2 mM Ca^{2+} . Each data point is the average difference in polar contacts relative to Vn-Na at 30°C. (B) Probability distributions of atomic distances between representative residues with polar contacts enhanced by Ca^{2+} . Each distribution reflects the average over the last 500 ns of five independent 1 μ s MD simulations. (C) Representative residues (*sticks*) with polar contacts that are affected by Ca^{2+} Structural model color scheme as in Fig. 1. (D) Probability distribution of water residence time within 5 Å of the m1 metal ion (average over five independent 1 μ s MD simulations). To see this figure in color, go online.

Role of rim-Asp in calcium-induced stabilization

To understand which residues of Vn are important for calcium-specific stabilization, we compared its amino acid sequence (Fig. S5) with the HX domains of two matrix metalloproteases (mmps)—mmp-14, which does not bind Ca²⁺ (43), and mmp-19, which binds Ca²⁺ and also gains thermal stability (44). In the sequence of mmp-14, the rim-Asp of repeats HX2 and HX4 are substituted with Asn and Gly, while those of mmp-19 are conserved, with the exception of HX4, where Asp is replaced by Ser. Moreover, mmp-19 shares other amino acid identities with Vn residues that form polar contacts in the Ca²⁺-bound protein (R176, E185, D248, R324, and Q345).

Based on this analysis, we performed MD simulations of three Vn-HX mutants: one where all four rim-Asp were mutated to Asn (mutant mD), and two where the rim-Asp were mutated as channel-juxtaposed pairs in HX1 and HX3 (mutant mD13: D162N and D255N) or HX2 and HX4 (mutant mD24: D207N and D347N). Five independent MD simulations for each mutant (Table S3), at 30°C, indicate that Ca²⁺ remains associated with the protein over the course of 1 μ s (Fig. S6). In all mutants, Ca²⁺ binds slightly higher above the channel ($\sim 0.1 \text{ Å}$) than wild-type, and the occluded ions and D166 side chain exhibit a broader range of conformational dynamics. These mutants also exhibit broader ranges of flexibility and compactness parameters than wild-type Vn-Ca (Fig. S3). Notably, the number of polar contacts in all three mutants is either slightly lower (mD13, mD24) or much lower (mD) than wild-type Vn-Na and appreciably lower than wild-type Vn-Ca (Fig. 4 A; Table S4). Taken together, the MD data suggest that the rim-Asp are important for the calcium-induced stabilization of Vn.

To assess the effects of these mutations experimentally, we prepared purified proteins and examined their conformational fitness, Ca²⁺-binding affinity, and thermodynamic stability by means of NMR and DSF. The NMR spectra show that the mutations do not disrupt the global fold of the protein, notwithstanding chemical shift differences from residues near the mutation sites, apparent especially for G177, G224, G276, and G441(Figs. 5 A-D and S6). The NMR spectrum of mD has very broad, poorly resolved lines that reflect a high degree of conformational exchange on the ms timescale. Its general resemblance to the wildtype spectrum suggests that the overall fold is maintained, but its high propensity for precipitation precluded Ca²⁺binding analysis by NMR. The spectra of mD13 and mD24, by contrast, have narrow, homogeneous, and wellresolved lines. In both cases, the addition of Ca²⁺ induces chemical shift perturbations similar to those observed for wild-type and consistent with Ca²⁺ association at the top of the channel. The data indicate that mD13 and mD24 have not lost the Ca²⁺-binding ability, in line with the MD

As we reported for wild-type Vn-HX (23), the addition of CaCl₂ to the mD13 and mD24 mutants induces the growth of a second set of NMR signals, which gain intensity with increasing CaCl₂ concentration (Fig. S7), in line with slow exchange (>ms) between Ca²⁺-bound and Ca²⁺-free protein. By measuring the change in NMR ¹H/¹⁵N signal height as a function of Ca²⁺ concentration for each of six well-resolved signals, we derived Ca²⁺-binding isotherms (Fig. S7) with average values of the apparent equilibrium

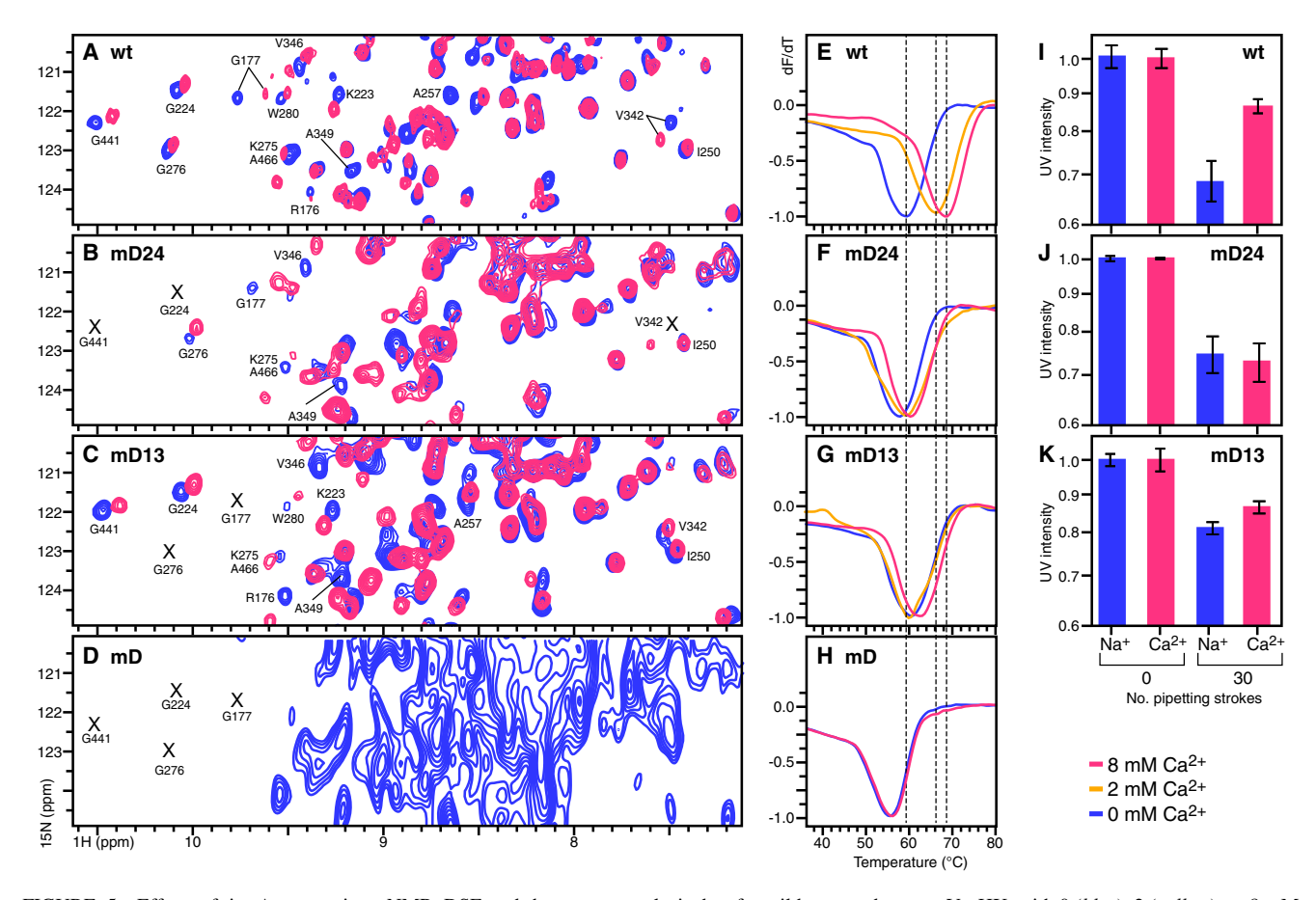


FIGURE 5 Effects of rim-Asp mutations. NMR, DSF, and shear-stress analysis data for wild-type and mutant Vn-HX, with 0 (blue), 2 (yellow), or 8 mM CaCl₂ (pink). (A-D) Selected regions of 2D solution NMR ¹H/¹⁵N HSQC spectra. Missing peaks resulting from the effects of rim-Asp mutagenesis are marked X. (E-H) Representative DSF traces. (I-K) Shear-stress analysis. The intensity of UV absorbance at 280 nm reflects the percentage of protein remaining in solution after 60 passes through the 0.21 mm diameter needle. Error bars reflect standard deviation for 6-18 independent experiments. To see this figure in color, go online.

dissociation constant (K_D) of 2.2 \pm 1.1 mM for mD13 and 0.8 ± 0.4 mM for mD24 (Table S6). These values are significantly greater than the apparent K_D of 27 \pm 1.5 μ M measured for wild-type protein (23) and reflect greatly reduced Ca²⁺-binding affinities of the mutants relative to wild type.

In line with the mutants' reduced affinities for Ca²⁺, the DSF data (Fig. 5 E-H; Table S5) show that the Ca²⁺induced thermal adaptability property is also significantly reduced in the three mutants compared with wild-type. Moreover, the mD mutant has lower thermal stability than wild-type in either Na⁺ or Ca²⁺. Notably, these results correlate with the loss of polar contacts predicted by the MD simulations for the mutants (Fig. 4 A; Tables S4 and \$5).

Calcium protects Vn from shear stress

Finally, we sought to explore the potential significance of the Ca²⁺ association with Vn in physiology, where extreme temperature excursions like those tested in this study do not occur, and temperature is maintained within the narrow homeostatic range near 37°C. In the vasculature, proteins are subject to hydrodynamic shear rates of 500–1000 s⁻¹ (45), and hydrodynamic flow can induce protein remodeling, unfolding, and aggregation. In this setting, the ability to adapt to changes in shear force acquires importance. For example, the von Willebrand factor, which also circulates in the highshear environment of the vasculature, binds Ca²⁺ via its A2 domain to resist shear-induced unfolding and cleavage by the mmp ADAMTS-13 (46,47).

To test whether Ca2+ can protect Vn-HX against shear stress, we performed an assay that estimates the amount of protein aggregated out of solution after multiple passes through a narrow diameter (0.21 mm) needle, as described (28). The 12 μ M (0.25 μ g/mL) protein solution is in the range of the physiological concentration of Vn (0.2-0.5 mg/mL), and we estimate that each pass of 150 μ L s⁻¹ through the needle generates a shear rate of \sim 165,000 s⁻¹ (48). This value is much greater than the hydrodynamic shear rates in human vasculature, although the time exposure to shear force in the experiment is much lower than

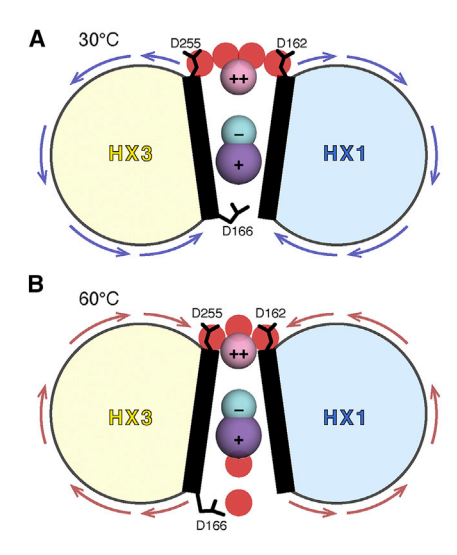


FIGURE 6 Model for the calcium-mediated temperature adaption of Vn-HX. (A) Adaptability to 30° C. (B) Adaptability to 60° C. To see this figure in color, go online.

the continuous hydrodynamic flow of the vasculature. After sixty passes through the needle (Fig. 5 I–K), the soluble concentration of wild-type HX, estimated by measuring UV absorbance at 280 nm, is ~20% greater with Ca^{2+} than with Na^+ , while no changes were observed when the protein solutions were incubated without pipetting in the spectrophotometer cuvette over the same time period. In the mD24 and mD13 mutants, by contrast, the level of soluble protein does not appear to be affected by Ca^{2+} and is reduced to an approximately equal extent in either Ca^{2+} or Na^+ after shearing. Overall, the response to shear force mirrors the response to temperature, and we conclude that Ca^{2+} cooperates with the four rim-Asp to protect Vn-HX against shear.

CONCLUSIONS

In summary, we have resolved the Ca²⁺-bound structure of the Vn-HX domain and described how Ca²⁺ enables the protein to adapt to large excursions of temperature and mechanical shear force. The crystal structures and MD simulations indicate that Ca²⁺ stabilizes multiple conformational states, enabling the protein to adapt its conformation according to environmental conditions. The four rim-Asp that form an electronegative corral at the top of the Vn-HX β-propeller are required for the full Ca²⁺-binding affinity; they play an important role in the calcium-induced adaptability to temperature and shear force through their participation in a network of water-mediated and direct polar contacts with Ca²⁺ and other side chains. Ca²⁺ promotes a reorganization of polar contacts that relays from top to bottom of the HX propeller and is accompanied by a conformational change of the channel. The hydration sphere of Ca²⁺ appears to play an important role in the environmental adaptation of Vn-HX.

The data suggest a model for the way in which Vn-HX adapts to its environment. At 30°C (Fig. 6 A), the top of the β1 strands splay apart to accommodate a Ca²⁺ ion and the additional water molecules in its coordination sphere. This results in a conformational rearrangement of polar contacts that propagates from the Ca²⁺-binding site at the top of the channel, around the propeller exterior, and all the way to the channel bottom. At 60°C, by contrast (Fig. 6 B), increased exchange of the Ca²⁺ hydration shell with bulk water reduces the effective number of water molecules that coordinate Ca²⁺. This loss of water is compensated by the electronegative rim-Asp carboxylates, which rearrange to make closer contact with the positively charged Ca²⁺ center, causing the top of the channel to constrict. In the rim-Asp mutants, this compensatory effect is impaired, the Ca²⁺-binding affinity is reduced, and the ability to adapt to temperature and mechanical stress is lost. While the precise types of conformational changes that operate under shear remains to be determined, the Ca²⁺-induced adaptability property is likely to play an important role for the activity of Vn in blood.

Unlike the large rearrangements observed for archetypal Ca²⁺ binding proteins, such as concanavalin, calmodulin, and troponin C (37), the calcium-induced conformational changes observed for the HX domain of Vn are subtle. Nevertheless, the formation of just a few polar contacts arising from small rearrangements has been shown to result in sufficient differences in stabilization free energy that protect proteins against extremes of temperature and pressure (40–42). For example, a stabilization free-energy difference in the range of 5 kcal/mol can be readily attained by forming a few polar H-bonds or as little as two salt bridges.

Ca²⁺ appears to be the ideally suited for promoting a protein's adaptability to environment. Its valency, polarizability, and ionic radius, as well as its hydration energy, hydrated radius, and related charge density, all make Ca²⁺ highly adaptable to sites of irregular coordination geometry, such as those of the Vn-HX domain (37). The coordination flexibility of Ca²⁺ is reflected in its variable coordination number (typically 6–8 and up to 12), coordination geometry, and bond lengths (2.2–2.4 Å). By contrast, the coordination geometry of Na⁺ is less flexible because its lower charge density (~2 times less than Ca²⁺) and hydration energy (~4 times less than Ca²⁺) restrict the coordination number (typically 4–6 with octahedral geometry).

Vn is a known regulator of osteoclast bone resorption (49), and Ca^{2+} has been shown to play a role in the interaction of Vn with the leukocyte integrin $\alpha_M\beta_2$ (Mac-1), independent of either the Vn RGD motif or somatomedin-B domain (50). Moreover, the association of Vn with Ca^{2+} is central in the ectopic calcified protein-lipid deposits associated with age-related macular degeneration and other degenerative pathologies. We propose that Ca^{2+} plays an

important role in adapting Vn to the diverse environments where it functions.

DATA AND MATERIALS AVAILABILITY

All data needed to evaluate the conclusions are present in the paper and/or the supporting material. Additional data are available upon request.

SUPPORTING MATERIAL

Supporting material can be found online at https://doi.org/10.1016/j.bpj. 2022.08.044

AUTHOR CONTRIBUTIONS

Y.T., K.S., A.E.A., W.I., and F.M.M. performed research. Y.T., K.S., A.E.A., W.I., and F.M.M. analyzed the data. Y.T. and F.M.M. wrote the paper. Y.T., W.I., and F.M.M. designed the research.

ACKNOWLEDGMENTS

This study was supported by grants from the National Institutes of Health (GM 118186 and CA030199), the National Science Foundation (MCB1810695), and the Canadian Institutes of Health Research (201711MFE-395794-210656) and a postdoctoral award from the Sanford Burnham Prebys Fishman Fund.

DECLARATION OF INTERESTS

Authors declare no conflict of interest.

REFERENCES

- Tomasini, B. R., and D. F. Mosher. 1991. Vitronectin. Prog. Hemost. Thromb. 10:269–305.
- Preissner, K. T., and U. Reuning. 2011. Vitronectin in vascular context: facets of a multitalented matricellular protein. *Semin. Thromb. Hemost.* 37:408–424.
- 3. Leavesley, D. I., A. S. Kashyap, ..., Z. Upton. 2013. Vitronectin–master controller or micromanager? *IUBMB Life*. 65:807–818.
- Yoneda, A., H. Ogawa, ..., I. Matsumoto. 1998. Characterization of the ligand binding activities of vitronectin: interaction of vitronectin with lipids and identification of the binding domains for various ligands using recombinant domains. *Biochemistry*. 37:6351–6360.
- Vaisar, T., S. Pennathur, ..., J. W. Heinecke. 2007. Shotgun proteomics implicates protease inhibition and complement activation in the antiinflammatory properties of HDL. J. Clin. Invest. 117:746–756.
- Gebb, C., E. G. Hayman, ..., E. Ruoslahti. 1986. Interaction of vitronectin with collagen. J. Biol. Chem. 261:16698–16703.
- Pytela, R., M. D. Pierschbacher, and E. Ruoslahti. 1985. A 125/115kDa cell surface receptor specific for vitronectin interacts with the arginine-glycine-aspartic acid adhesion sequence derived from fibronectin. *Proc. Natl. Acad. Sci. USA*. 82:5766–5770.
- Zhou, A., J. A. Huntington, ..., R. J. Read. 2003. How vitronectin binds PAI-1 to modulate fibrinolysis and cell migration. *Nat. Struct. Biol.* 10:541–544.
- Podack, E. R., K. T. Preissner, and H. J. Müller-Eberhard. 1984. Inhibition of C9 polymerization within the SC5b-9 complex of complement by S-protein. *Acta Pathol. Microbiol. Immunol. Scand. Suppl.* 284:89–96.

- Singh, B., Y. C. Su, and K. Riesbeck. 2010. Vitronectin in bacterial pathogenesis: a host protein used in complement escape and cellular invasion. *Mol. Microbiol.* 78:545–560.
- Anderson, D. H., G. S. Hageman, ..., L. V. Johnson. 1999. Vitronectin gene expression in the adult human retina. *Invest. Ophthalmol. Vis. Sci.* 40:3305–3315.
- Hageman, G. S., R. F. Mullins, ..., D. H. Anderson. 1999. Vitronectin is a constituent of ocular drusen and the vitronectin gene is expressed in human retinal pigmented epithelial cells. FASEB J. 13:477–484.
- 13. Ozaki, S., L. V. Johnson, ..., D. H. Anderson. 1999. The human retina and retinal pigment epithelium are abundant sources of vitronectin mRNA. *Biochem. Biophys. Res. Commun.* 258:524–529.
- Walker, D. G., and P. L. McGeer. 1998. Vitronectin expression in Purkinje cells in the human cerebellum. *Neurosci. Lett.* 251:109–112.
- Dufourcq, P., H. Louis, ..., J. Bonnet. 1998. Vitronectin expression and interaction with receptors in smooth muscle cells from human atheromatous plaque. Arterioscler. Thromb. Vasc. Biol. 18:168–176.
- Ekmekci, H., H. Sonmez, ..., E. Kokoglu. 2002. Plasma vitronectin levels in patients with coronary atherosclerosis are increased and correlate with extent of disease. *J. Thromb. Thrombolysis*. 14:221–225.
- 17. Zhang, R., L. Barker, ..., G. Jackowski. 2004. Mining biomarkers in human sera using proteomic tools. *Proteomics*. 4:244–256.
- Shin, T. M., J. M. Isas, ..., J. Chen. 2008. Formation of soluble amyloid oligomers and amyloid fibrils by the multifunctional protein vitronectin. *Mol. Neurodegener*. 3:16.
- Luibl, V., J. M. Isas, ..., J. Chen. 2006. Drusen deposits associated with aging and age-related macular degeneration contain nonfibrillar amyloid oligomers. J. Clin. Invest. 116:378–385.
- Mullins, R. F., S. R. Russell, ..., G. S. Hageman. 2000. Drusen associated with aging and age-related macular degeneration contain proteins common to extracellular deposits associated with atherosclerosis, elastosis, amyloidosis, and dense deposit disease. FASEB J. 14:835–846.
- Bergen, A. A., S. Arya, ..., I. Lengyel. 2019. On the origin of proteins in human drusen: the meet, greet and stick hypothesis. *Prog. Retin. Eye Res.* 70:55–84.
- Shin, K., B. C. Lechtenberg, ..., F. M. Marassi. 2019. Structure of human Vitronectin C-terminal domain and interaction with Yersinia pestis outer membrane protein Ail. Sci. Adv. 5:eaax5068.
- Shin, K., J. E. Kent, ..., F. M. Marassi. 2020. Calcium and hydroxyapatite binding site of human vitronectin provides insights to abnormal deposit formation. *Proc. Natl. Acad. Sci. USA*. 117:18504–18510.
- Winn, M. D., C. C. Ballard, ..., K. S. Wilson. 2011. Overview of the CCP4 suite and current developments. *Acta Crystallogr. D Biol. Crystallogr.* 67 (Pt 4):235–242.
- Emsley, P., B. Lohkamp, ..., K. Cowtan. 2010. Features and development of Coot. Acta Crystallogr. D Biol. Crystallogr. 66 (Pt 4):486–501.
- Murshudov, G. N., P. Skubák, ..., A. A. Vagin. 2011. REFMAC5 for the refinement of macromolecular crystal structures. *Acta Crystallogr. D Biol. Crystallogr.* 67 (Pt 4):355–367.
- Chen, V. B., W. B. Arendall, 3rd, ..., D. C. Richardson. 2010. MolProbity: all-atom structure validation for macromolecular crystallography. *Acta Crystallogr. D Biol. Crystallogr.* 66 (Pt 1):12–21.
- Dobson, J., A. Kumar, ..., D. J. Brockwell. 2017. Inducing protein aggregation by extensional flow. *Proc. Natl. Acad. Sci. USA*. 114:4673–4678.
- Hamad, N., R. Yoneda, ..., M. Katahira. 2021. Non-coding RNA suppresses FUS aggregation caused by mechanistic shear stress on pipetting in a sequence-dependent manner. Sci. Rep. 11:9523.
- Singh, C., H. Lee, ..., F. M. Marassi. 2020. Mutually constructive roles of Ail and LPS in Yersinia pestis serum survival. *Mol. Microbiol*. 114:510–520.
- 31. Brooks, B. R., C. L. Brooks, 3rd, ..., M. Karplus. 2009. CHARMM: the biomolecular simulation program. *J. Comput. Chem.* 30:1545–1614.

- 32. Jorgensen, W. L., J. Chandrasekhar, ..., M. L. Klein. 1983. Comparison of simple potential functions for simulating liquid water. J. Chem. Phys. 79:926-935.
- 33. Jo, S., T. Kim, ..., W. Im. 2008. CHARMM-GUI: a web-based graphical user interface for CHARMM. J. Comput. Chem. 29:1859-1865.
- 34. Ko, J., D. Lee, H. Park, ..., C. Seok. 2011. The FALC-Loop web server for protein loop modeling. Nucleic Acids Res. 39:W210-W214.
- 35. Eastman, P., M. S. Friedrichs, ..., V. S. Pande. 2013. OpenMM 4: a Reusable, Extensible, hardware independent library for high performance molecular simulation. J. Chem. Theor. Comput. 9:461-469.
- 36. Zheng, H., D. R. Cooper, ..., W. Minor. 2017. CheckMyMetal: a macromolecular metal-binding validation tool. Acta Crystallogr. D Struct. Biol. 73 (Pt 3):223-233.
- 37. Carafoli, E., and J. Krebs. 2016. Why calcium? How calcium became the best communicator. J. Biol. Chem. 291:20849-20857.
- 38. Meinhold, L., J. C. Smith, ..., A. H. Zewail. 2007. Picosecond fluctuating protein energy landscape mapped by pressure temperature molecular dynamics simulation. Proc. Natl. Acad. Sci. USA. 104:17261-17265.
- 39. Kumar, S., C. J. Tsai, and R. Nussinov. 2000. Factors enhancing protein thermostability. $Protein\ Eng.\ 13:179-191.$
- 40. Dill, K. A. 1990. Dominant forces in protein folding. Biochemistry. 29:7133-7155.
- 41. Vogt, G., S. Woell, and P. Argos. 1997. Protein thermal stability, hydrogen bonds, and ion pairs. J. Mol. Biol. 269:631-643.

- 42. Rees, D. C., and A. D. Robertson. 2001. Some thermodynamic implications for the thermostability of proteins. Protein Sci. 10:1187–1194.
- 43. Zhao, Y., T. C. Marcink, ..., S. R. Van Doren. 2015. Transient collagen triple helix binding to a key metalloproteinase in invasion and development. Structure. 23:257-269.
- 44. Mysliwy, J., A. J. Dingley, ..., J. Grötzinger. 2006. Structural characterization and binding properties of the hemopexin-like domain of the matrixmetalloproteinase-19. Protein Expr. Protein Expr. Purif. 46:406-413.
- 45. Ruggeri, Z. M., and G. L. Mendolicchio. 2007. Adhesion mechanisms in platelet function. Circ. Res. 100:1673-1685.
- 46. Zhou, M., X. Dong, ..., J. Ding. 2011. A novel calcium-binding site of von Willebrand factor A2 domain regulates its cleavage by ADAMTS13. Blood. 117:4623-4631.
- 47. Jakobi, A. J., A. Mashaghi, ..., E. G. Huizinga. 2011. Calcium modulates force sensing by the von Willebrand factor A2 domain. Nat. Commun. 2:385.
- 48. Bekard, I. B., P. Asimakis, ..., D. E. Dunstan. 2011. The effects of shear flow on protein structure and function. *Biopolymers*. 95:733–745.
- 49. Chambers, T. J., and K. Fuller. 2011. How are osteoclasts induced to resorb bone? Ann. N. Y. Acad. Sci. 1240:1-6.
- 50. Kanse, S. M., R. L. Matz, ..., K. Peter. 2004. Promotion of leukocyte adhesion by a novel interaction between vitronectin and the beta2 integrin Mac-1 (alphaMbeta2, CD11b/CD18). Arterioscler. Thromb. Vasc. Biol. 24:2251-2256.